Supplementary Information

1 Overview previous work

In Table S1 an overview of state-of-the-art work on localized highly concentrated electrolytes is presented, together with the information regarding the here studied non-flammable liquid electrolytes.

Table S1. Overview the electrolyte systems of this and previous studies on localized highly concentrated electrolytes.

Electrolyte	Anode	Cathode	Conductivity (mS/cm)	Cut-off potentials (V)	Current density (mA/cm²)	Discharge capacity (mAh/g)	Cycles (#)	Ref.
1.5 M LiFSI in TEP/BTFE	Gr (2.4 mAh cm^{-2}) Cu	NMC622 (2.0 mAh cm^{-2}) Li	1.97	3.0 – 4.2	0.1 C	1 mAh cm^{-2}	N/A	This work
1.5 M LiFSI in TEP/TTE	Gr (2.4 mAh cm^{-2}) Cu	NMC622 (2.0 mAh cm^{-2}) Li	1.57	3.0 – 4.2	0.1 C	1 mAh cm^{-2}	100	This work
1.2 M LiFSI in TEP/ BTFE	Li	NMC622 (1.6 mAh cm^{-2})	1.29	2.8 – 4.4	1.6 mA cm^{-2} (1 C)	180	600	1
1.2 M LiFSI in DMC/BTFE	Li	NMC111 (2.0 mAh cm^{-2})	2.67	2.7 – 4.3	2 mA cm^{-2} (1 C)	150	700	2
1.2 M LiFSI in EC/EMC/BTFE + 0.15 M LiDFOB	Li	NMC111 (3.8 mAh cm^{-2})	N/A	2.7 – 4.3	1 mA cm^{-2} (1 C)	115	100	3
1.2 M LiFSI/TEPa-EC-BTFE	Gr	NMC811	1.4	2.8 – 4.3	C/2 charge, 1 C discharge	134.8	300	4
1.2 M LiFSI in TEP/FEC/BTFE	Si-Gr (2.21 mAh cm^{-2}, 3.2 mAh cm^{-2})	NMC111 (1.9 mAh cm^{-2}, 2.8 mAh cm^{-2})	N/A	2.7–4.2	0.3 mA cm^{-2} charge, 0.75 mA cm^{-2} discharge (5 C)	134.7	600	5
1.2 M LiFSI-3TMS-3TTE	Li	NMC	2.03	2.7–4.3	0.5 mA cm^{-2} (C/3)	~150	300	6
1.5 M LiFSI-1.2DME-3TTE	Li	NMC811 (1.5 mAh cm^{-2})	2.44	2.8 – 4.4	C/10 C/3	180	300	7
1.4 M LiFSI DMC/EC/TTE	Gr	NMC811	1.07	2.5 – 4.4	3x C/20 C/10 1C (2.8 mA cm^{-2})	173	600	8
LiFSI DMAC TTE (1:1.3:2 by mol)	Li	NMC532	1.63	3.0 – 4.3	2x C/10, C/5	144	155	9
1.44 M LiFSI TMP/TTE/FEC (1.2:0.2:3 by mol)	Gr	NMC811	1	2.5 – 4.4	1x C/20, 2x C/10 C/3 charge, 1C discharge	145	500	10
1.57 M LiFSI DME/TTE/FEC	Gr	NMC811	1.75	2.5 - 4.4	1x C/20, 2x C/10 C/3 charge, 1C discharge (1.45 mA cm^{-2})	142.8	500	11

2 Raman Spectroscopy

In Figure S1 the Raman Spectroscopy results are shown for neat TEP, 1.5 M LiFSI in TEP and 3.0 M LiFSI in TEP, to elucidate at which concentration a so called highly concentrated electrolyte solvation structure is obtained. Neat TEP solvent shows a peak around 730 cm^{-1} which is attributed to the symmetric stretching vibration of P-O-(C), *i.e.* uncoordinated (or free) solvent. According to the theory this peak is slightly shifted to 740 cm^{-1} when the salt concentration is increased to 3.0 M LiFSI, due to enhanced Li^+-TEP solvation. However, this shift seems not to be very strong in this electrolyte. However, in the Raman spectrum of 1.5 M LiFSI in TEP this peak is split into two regions, indicating that TEP is present both as uncoordinated as well as free solvent. In Figure S2, the Raman Spectroscopy results are shown for the wavelength range between 500-1500 cm^{-1}. Figure S3 and S4 shows a more detailed insight in the P=O stretching vibration (1290 cm^{-1}) and CH_2 bending vibration (1450 cm^{-1}) of TEP, showing the effect of diluents on the Li-TEP solvation structure.

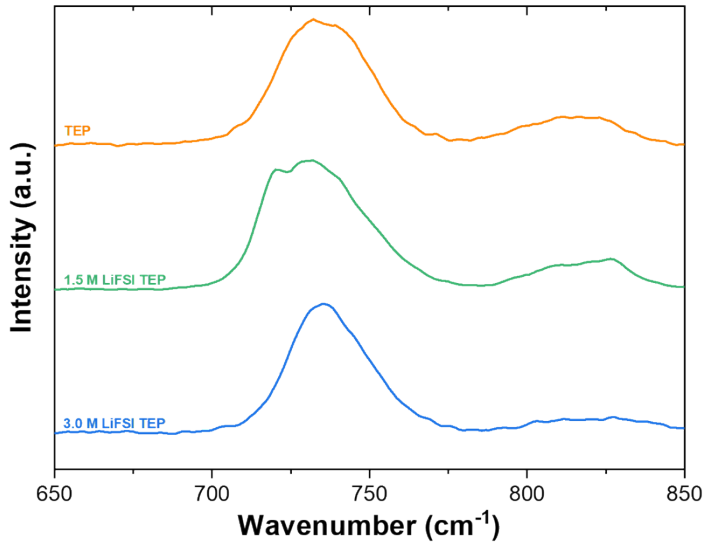

Figure S1. Raman spectroscopy of neat solvent TEP, 1.5 M LiFSI in TEP, 3.0 M LiFSI in TEP in the wavelength range of 650 cm^{-1} to 850 cm^{-1}. This figure highlights the effect of increasing the salt concentration.

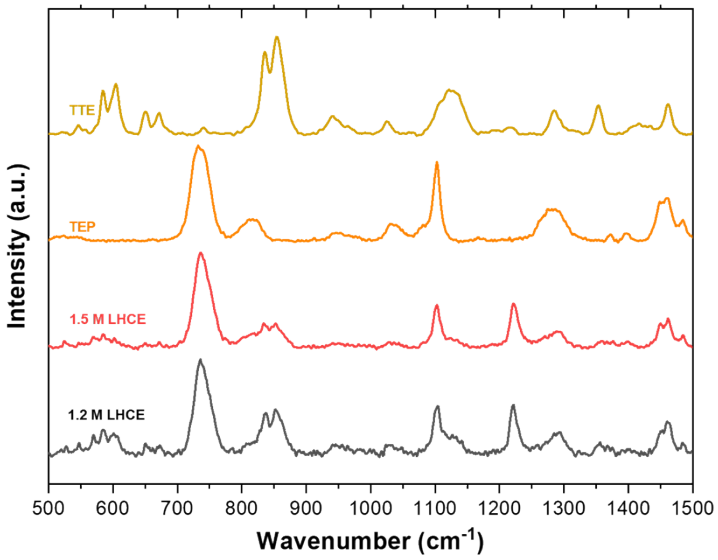

Figure S2. Raman spectroscopy of neat TTE, neat TEP, 1.5 M LiFSI in TEP/TTE, 1.2 M LiFSI in TEP/TTE in the wavelength range of 500 cm^{-1} to 1500 cm^{-1}.

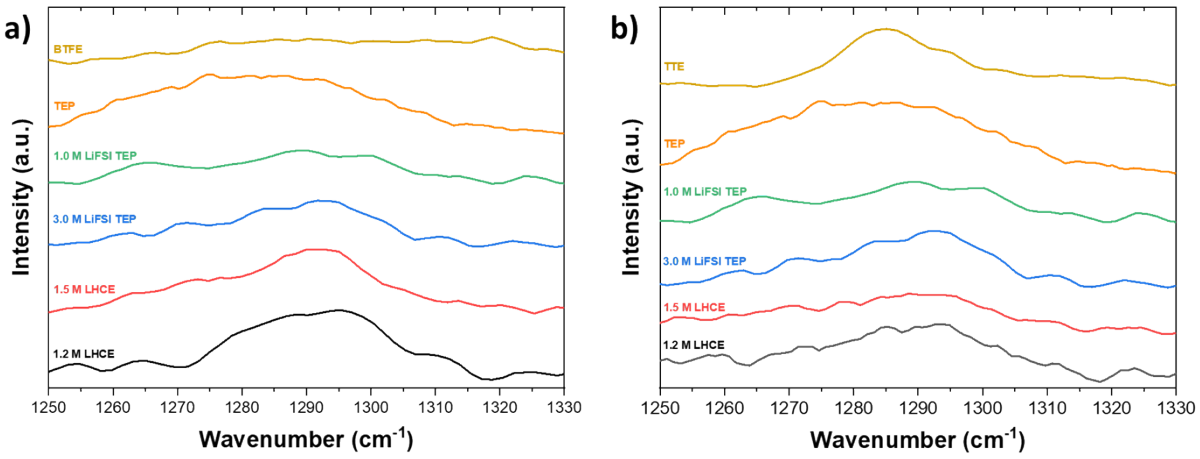

Figure S3. Raman spectroscopy of a) BTFE and b) TTE based electrolytes in the wavelength range of 1250 cm^{-1} to 1330 cm^{-1}.

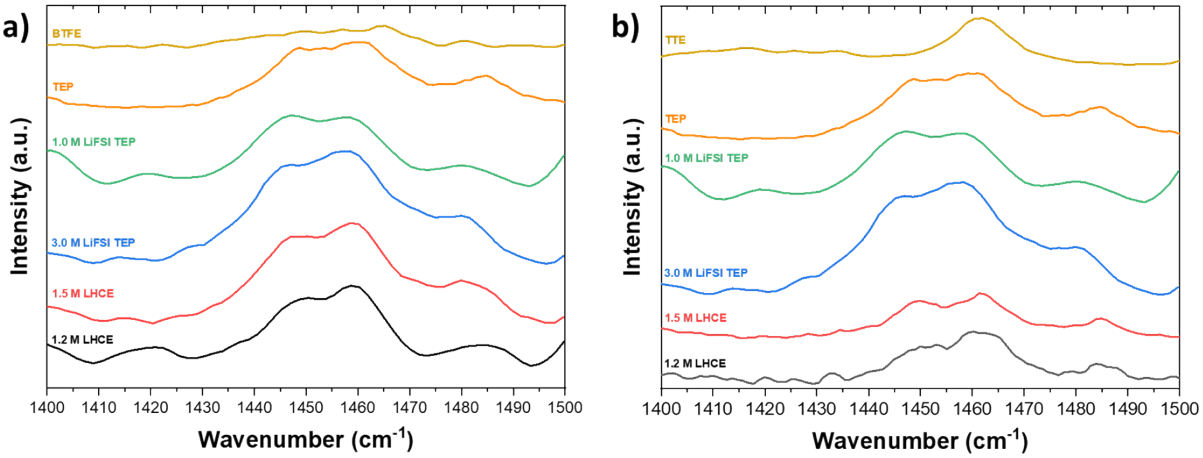

Figure S4. Raman spectroscopy of a) BTFE and b) TTE based electrolytes in the wavelength range of 1400 cm^{-1} to 1500 cm^{-1}.

3 ^{1}H-NMR, ^{7}Li-NMR ^{13}C-NMR and ^{19}F-NMR

In Figure S4 a complete overview of the ^{13}C-NMR spectra for the electrolytes used in this study is shown. In Figure S5 it is shown that the CF_3 group in BTFE is not experiencing any change in chemical shift when the content is increased. This indicates that this group is not engaging in the Li^+-TEP solvation structure. The same reasoning can be applied to the fluorinated carbon groups in TTE, where also no change is observed (or δ <0.1 ppm). In Figure S7, the ^{1}H-NMR spectroscopy results are shown for a) BTFE and b) TTE. In Figure SX and SXX the ^{19}F-NMR spectra for BTFE and TTE based electrolytes are shown, respectively. From these figures it is observed that the fluorine of FSI experiences a downfield shift upon increase in salt concentration, indicating an increased amount of ion pairing. If the BTFE based LHCEs are formed, the fluorine of FSI experiences minor changes in chemical shifts (δ <0.1 ppm). The fluorine groups of BTFE also experience a minor change when more diluent is added to obtain LHCEs. For the TTE based LHCEs the fluorine of FSI experience a more significant upfield shift upon adding the diluent ($\delta \approx 0.5$ ppm), indicating less strong interaction between FSI and Li^+. Most of the fluorine groups of TTE also experience marginal chemical shifts upon increasing diluent concentration in the LHCEs, except for the R-CF_2-O group which experiences a more significant chemical shift ($\delta > 0.1$ ppm), shown in figure SX d). This indicates either reduced interaction between TTE and Li^+, reduced interaction between the Li^+-TEP solvation sheath or enhanced interaction between TTE and FSI.

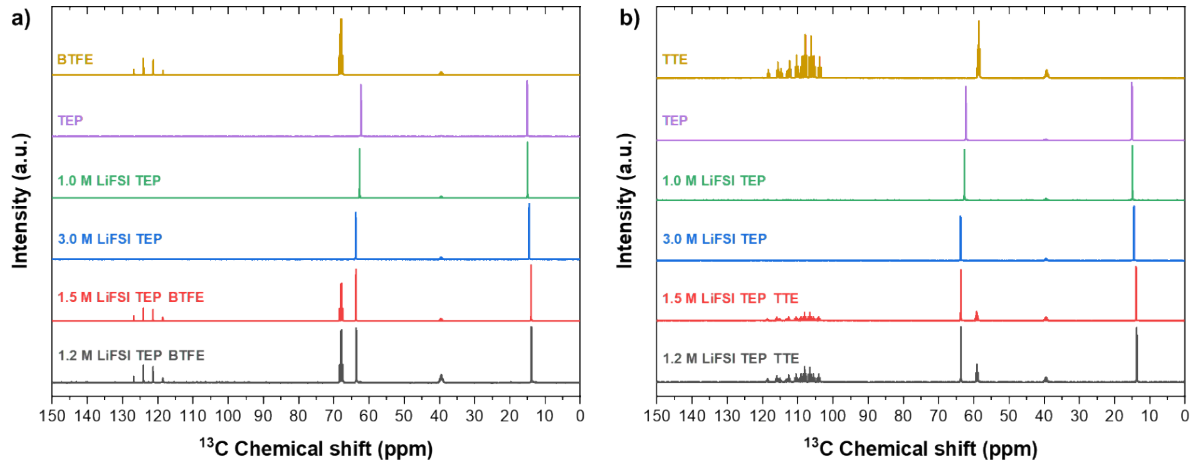

Figure S5. ^{13}C-NMR spectroscopy of LHCEs based on two different diluents in the range of 150 ppm to 0 ppm. The BTFE based electrolyte is shown in figure a) and the TTE based electrolyte is shown in figure b).

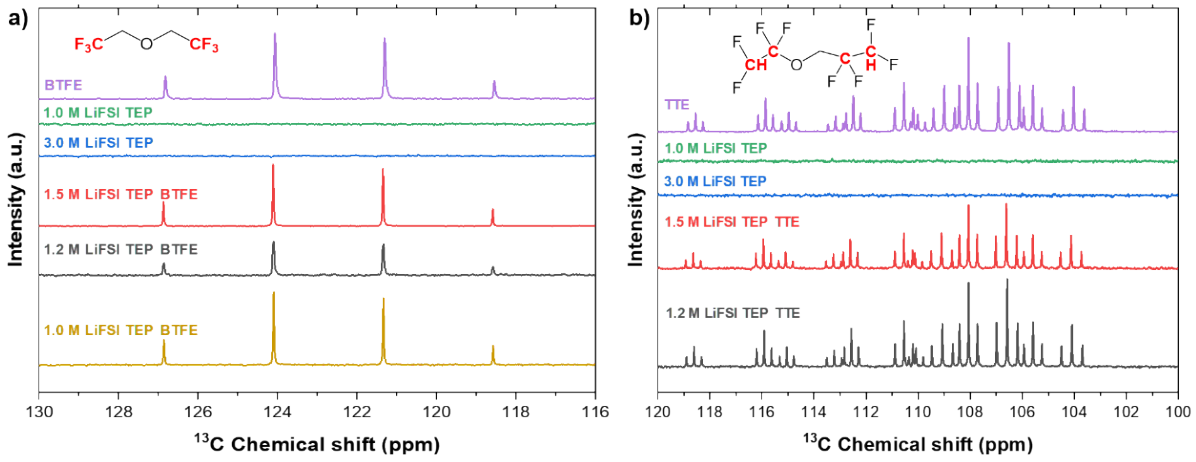

Figure S6. ^{13}C-NMR spectroscopy of the LHCEs based on BTFE and TTE, in the range of 130 ppm to 115 ppm and 120 ppm to 100 ppm, respectively. The peaks represent the red highlighted carbon groups in the molecular structure of the main solvents.

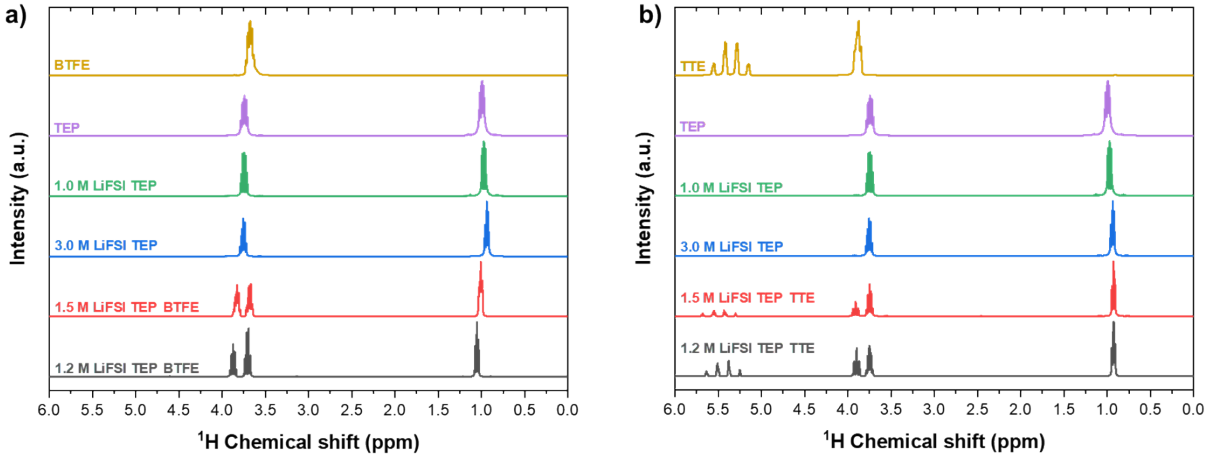

Figure S7. ^{1}H-NMR spectra of a) BTFE and b) TTE based electrolytes.

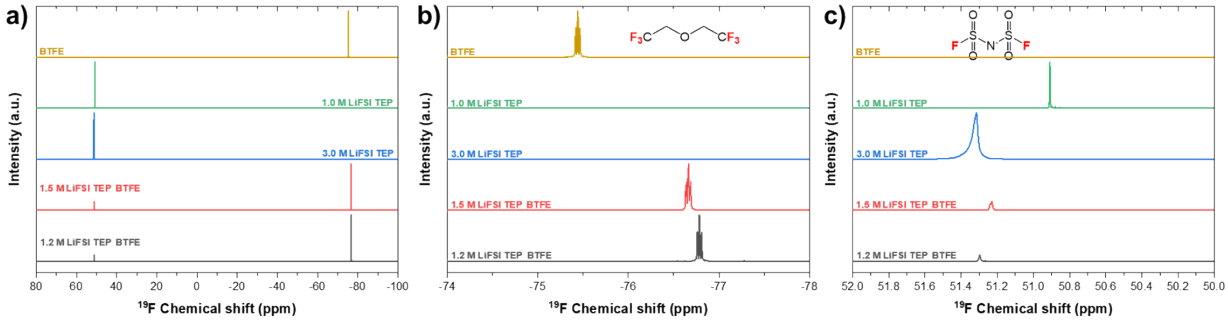

Figure S8. ^{19}F-NMR spectra of BTFE based electrolytes. a) the full spectrum, b) and c) chemical shifts for the fluorine group in BTFE and FSI, respectively.

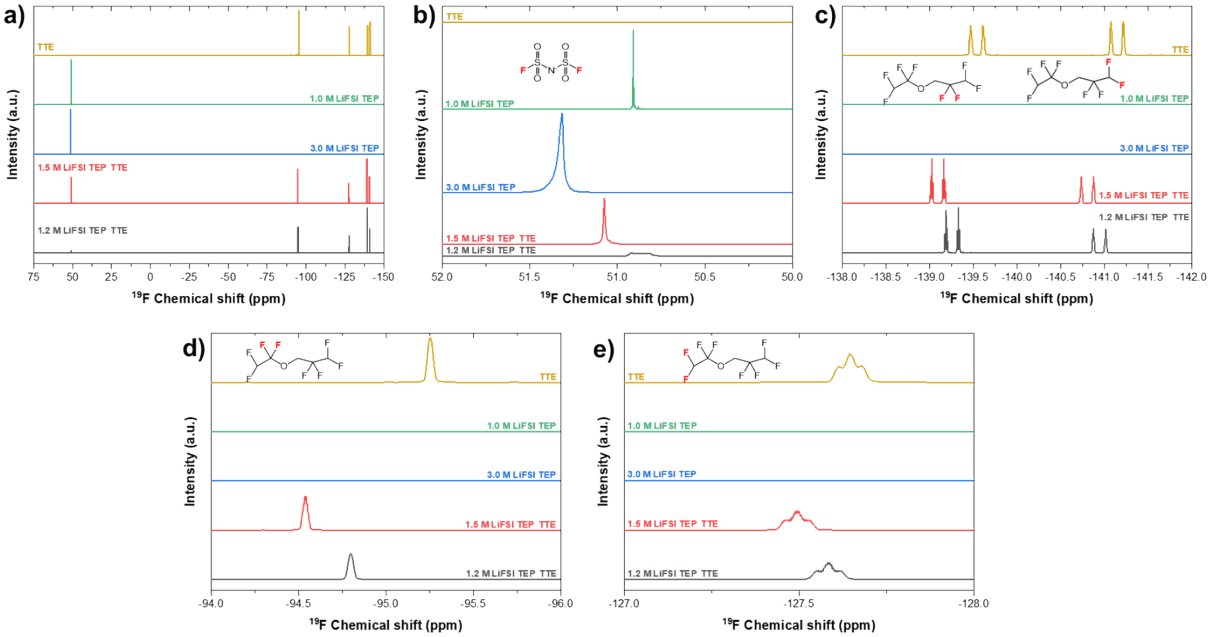

Figure S9. ^{19}F-NMR spectra of TTE based electrolytes. a) the full spectrum, b), c), d) and e) chemical shifts for specific fluorine groups.

4 Classical Molecular Dynamics

Figure S13 shows both the Coulomb (left-hand side) and LJ (right-hand side) interactions for LiFSI in pure TEP (a), and also diluted in TTE (b) and BTFE (c). Overall, the salt concentration increases the Coulombic attraction between Li^+ and both the anions and the TEP.

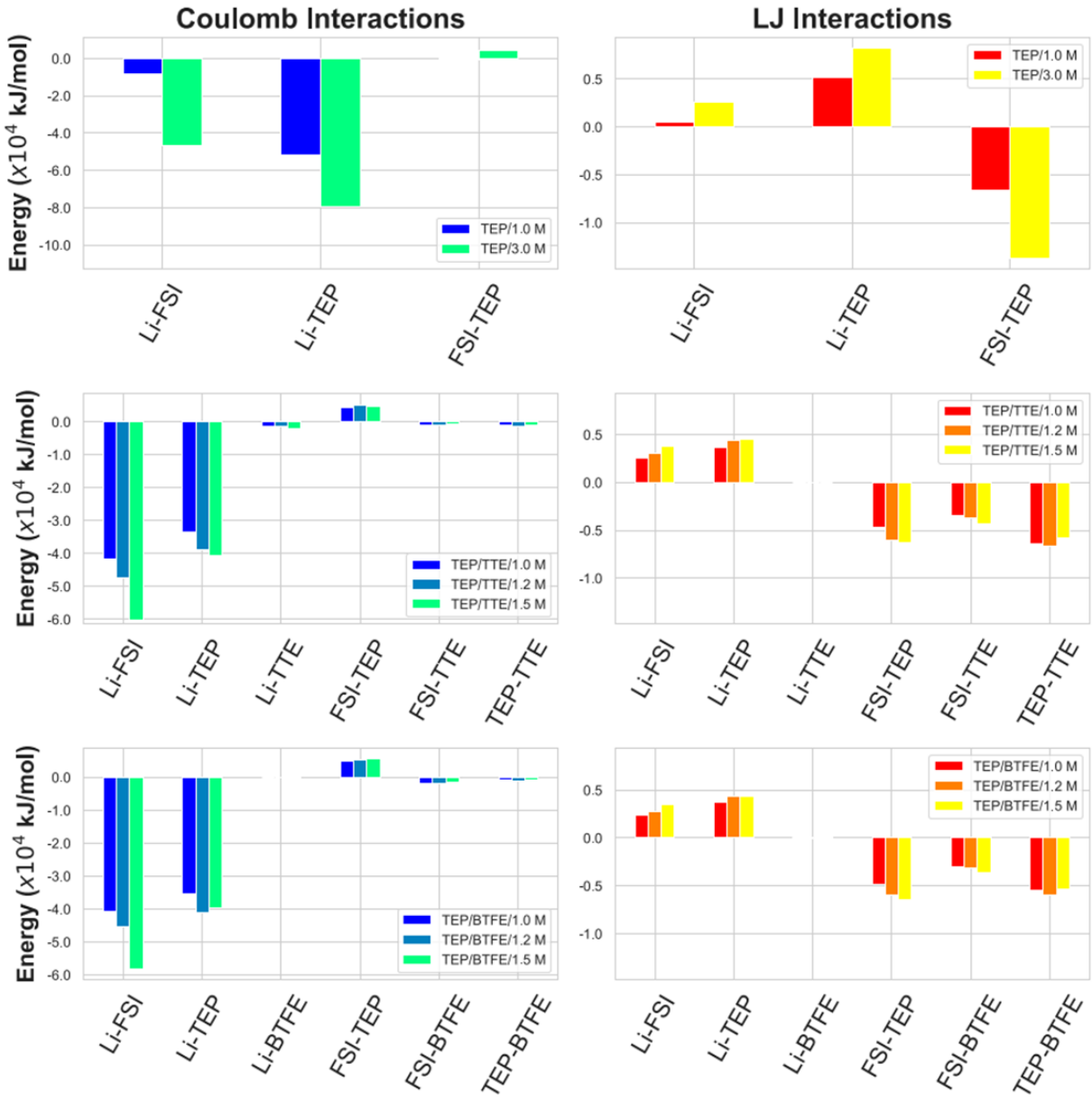

Figure S10. Coulomb (left) and LJ interactions (right) between Li+ cation and the anion, TEP, and either TTE or BTFE for different salt concentrations. Line a is for pure TEP, b for TTE diluent, and c for BTFE diluent.

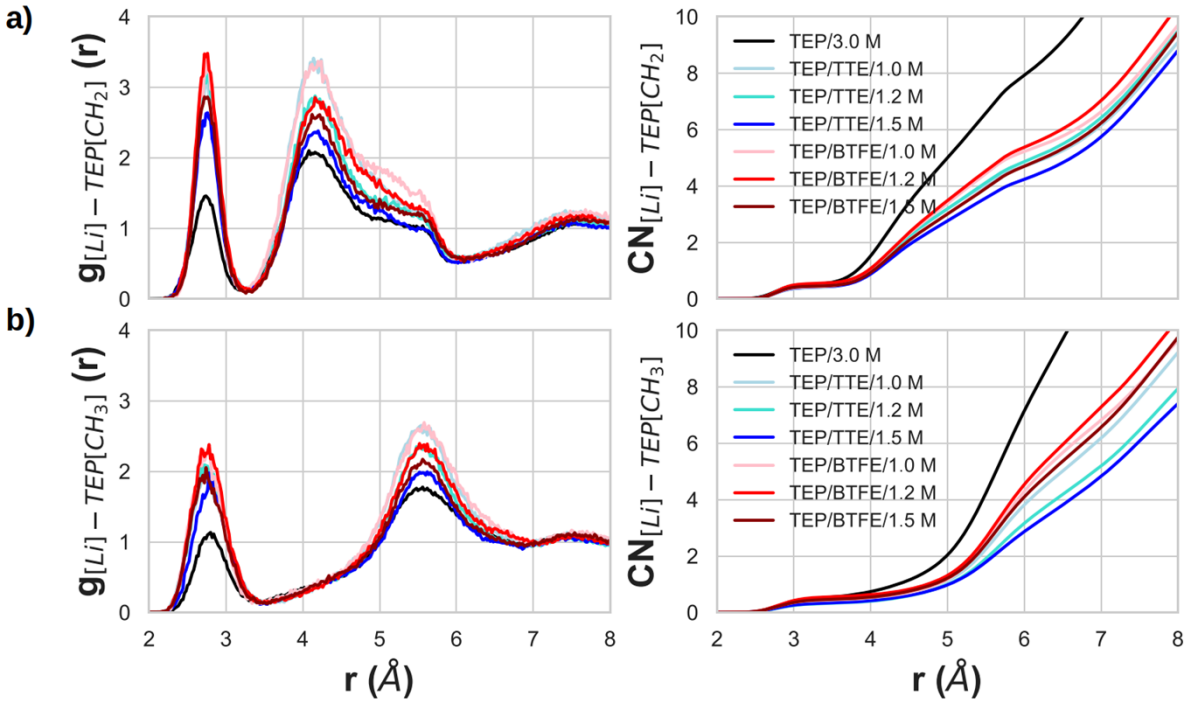

Figure S11. Plot a) shows the RDF along with the CN for Li^+ cation with respect to carbon atom of CH_2 of TEP, and plot b) similarly shows the results for CH_3 group. The black lines indicate the pure TEP.

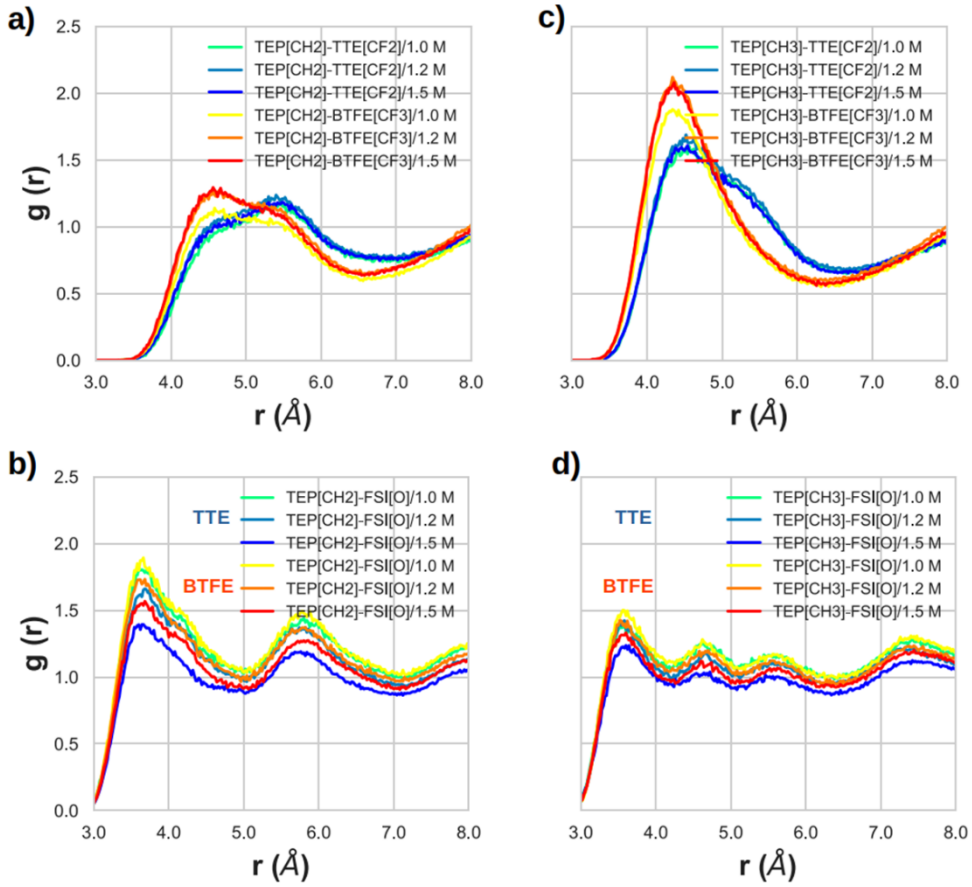

Figure S12. RDFs for TEP's CH_2 group (left) and TEP's CH_3 group (right). The graphs with shades of blue indicate TTE's CF_2 group and the graphs with shades of red BTFE's CF_3 groups.

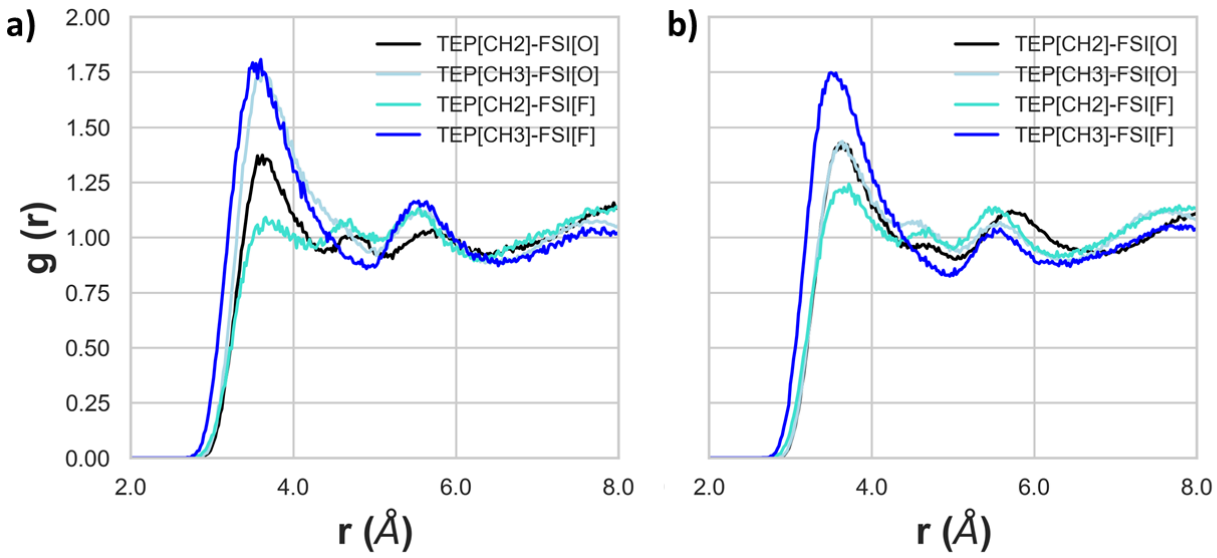

Figure S13. RDF of TEP's carbon groups with respect to both oxygen and fluorine of FSI^-. The left plot shows RDF for 1.0 M salt concentration, and the one on the right side, for 3.0 M. As one goes from conventional concentration to the high concentration, the interplay between fluorine and CH_3 becomes more highlighted.

The values for CH_2 in TTE and BTFE become 1 from 6.7 Å and 5.4 Å, respectively, regardless of the salt concentration, as can be seen in figures S17-a) and -b).

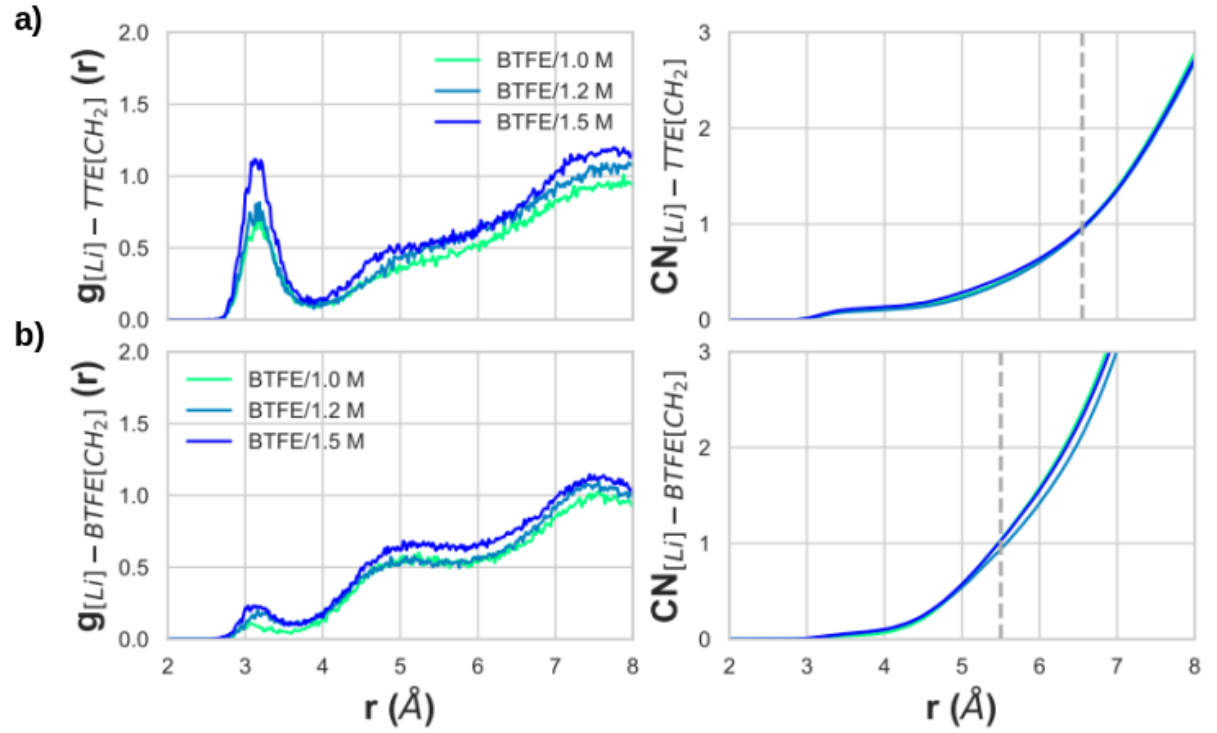

Figure S14. In a) the RDF for Li^+ with respect to the carbon atom of the CH_2 group of TTE and its respective CN plot are shown. In b) the plots for the BTFE based LHCE are shown. The vertical dashed lines in b) indicate the point at which the CN equals to 1.0.

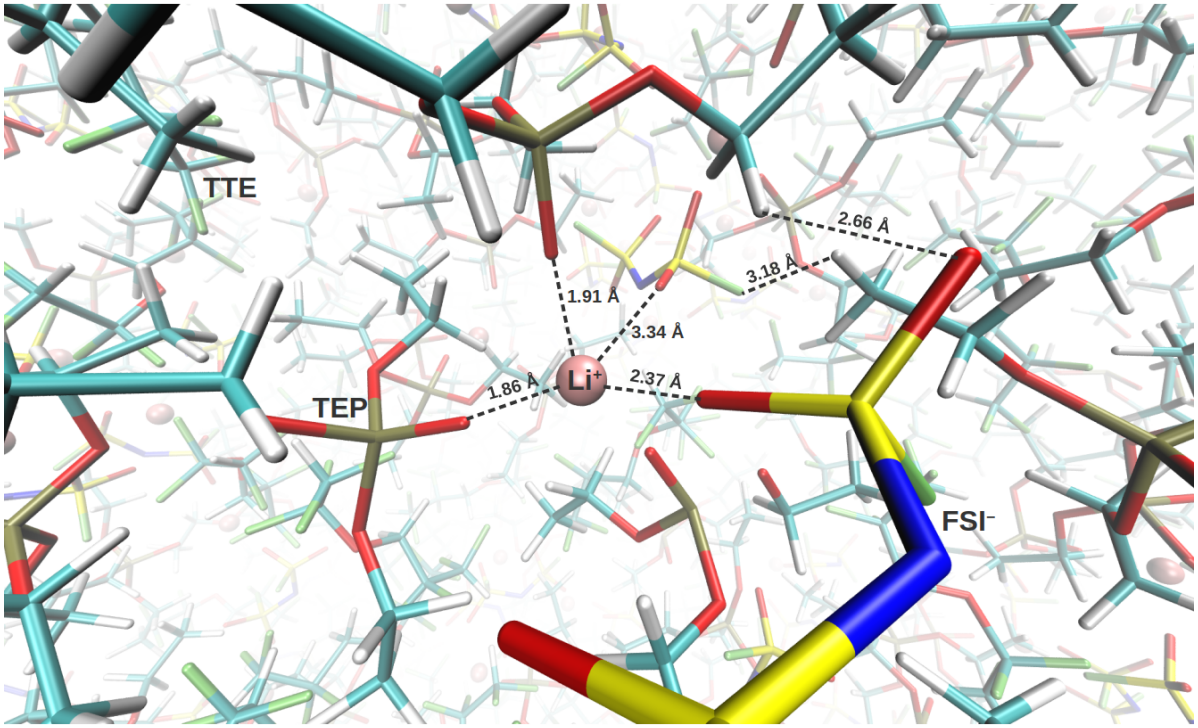

Figure S15. Visualization of the CIP and AGG formation in LHCE for TTE as diluent. The figure shows the atomic distance, indicated by dashed lines. White, red, yellow, lime, cyan and blue ellipsoids are for hydrogen, oxygen, sulfur, fluorine, carbon and nitrogen, respectively. It is possible to see that the diluent is surrounding the aggregation region.

5 Reduced density gradient (RDG)

The RDG, $s = 1/\left(2\left(3\pi^2\right)^{1/3}\right)|\nabla\rho|/\rho^{4/3}$, is a dimensionless quantity that describes the deviation from the homogeneous electron density. It has very large positive values for small electronic density (region where there is no interaction) and very small values for regions where there are both covalent and non-covalent interactions (NCI). The type of interaction depends on the Hessian (second derivative) of the electronic density, λ_2, and its sign indicates whether it is attractive or repulsive. If λ_2 and ρ are approximately null, the region is governed by van der Waals (VDW) interactions. If λ_2 is positive, the interactions are strongly repulsive (steric effects, for instance). Otherwise, the interactions are attractive (H- or halogen-bonds, for example).

Figure S19 shows the RDG for TEP (a), 1.0 M LiFSI in TEP (b), 3.0 M LiFSI in TEP (c), 1.5 M LiFSI in TEP/TTE (d), and 1.5 M LiFSI in TEP/BTFFE (e). The isosurfaces are set to s = 0.5 a.u., and their colors correspond to the colors of the scatter plots for each system. The importance of this kind of analysis relies on the visualization of regions where weak interactions play an important role in the analysis, for example, in the analysis of ^{13}C-NMR chemical shifts. The black arrows in Figure S18-b) through -e) indicate the most important interactions with respect to the experimental NMR results. Comparing figure S18 a) and b), where b) only shows van der Waals interactions with repulsive character between the CH_2 groups (bonded to O2) and O1, O3, or O4, there is an attractive interaction between FSI[S] and TEP[O2] (an oxygen bonded to CH_2 group). Also, amongst many VDW regions, the one that is indicated by the arrow is well localized between both FSI[F] and CH_2 and CH_3. The same can be seen for FSI[O]. The orange region, which mainly lies between FSI[O] and TEP[Os], corresponds to repulsive interaction. By increasing the salt concentration (figure c), the interaction between FSI[S] and TEP[O] changes from O2 to O1, but the intensity is similar. Furthermore, the disposition of the FSI oxygen and fluorine changes. For 1.0 M salt concentration, both fluorine points away from the FSI[S]-TEP[O2] interaction, leaving one oxygen from each sulfur interacting with CH_2 and CH_3 groups of O1. In the 3.0 M regime, one fluorine atom points to the TEP[O1], and is responsible for a local VDW interaction with both O1 and CH_3 group. The oxygen of the other sulfur atom in the FSI molecule, interacts also via VDW interaction with both CH_2 and CH_3 groups bonded to the same O1. There is also VDW interaction between the nitrogen and the CH_3 group. Those interplays change the electronic density from the carbon atoms of CH_2 groups towards the TEP's O1. This could be the reason for the downfield

shift observed for TEP's CH_2 from 1.0 M to 3.0 M. Also, the interaction between the FSI[F/O] and the carbon groups are maintained and, due to the different electronegativity between them, these are the interactions, along with the FSI[N]-CH_3 VDW interaction, that contribute to the upfield chemical shift of the CH_3 group.

By adding the diluent TTE (figure d), a strong attractive interaction appears between FSI[O] and the cation that is linked to the TEP[O4], which shows attractive interaction with TTE[H]. Because of the diluents, FSI[O] interacts only with CH_2 groups, while TTE[F] interacts with CH_3 groups, which contributes to NMR shifts observed in figure 4-d). It is also possible to see VDW interaction between FSI[F] and TTE[F]. Amidst the TEP molecules, one can see repulsive interactions between them. There is also (purple arrow) a mild attractive interaction between a TEP[O4] and a CH_2 group of the other TEP. When regarding the BTFE as diluent, the attractive interaction between FSI[S] and TEP[O] remains present (which is not observed for TTE), and it is stronger than in the conventional and high concentrated electrolytes (figures b and c). Also, an attractive interaction between the cation and TEP[O4] and the CH_2 of BTFE is also observed. A relatively attractive interaction is as well observed between the FSI[N] and CH_3. The same nitrogen also interacts with an oxygen of FSI which is bonded to a cation. Besides, many VDW and repulsive interactions are also seen between the TEP molecules and between TEP and BTFE fluorine atoms, as well as VDW interaction between the BTFE[F] and both CH_2 and CH_3.

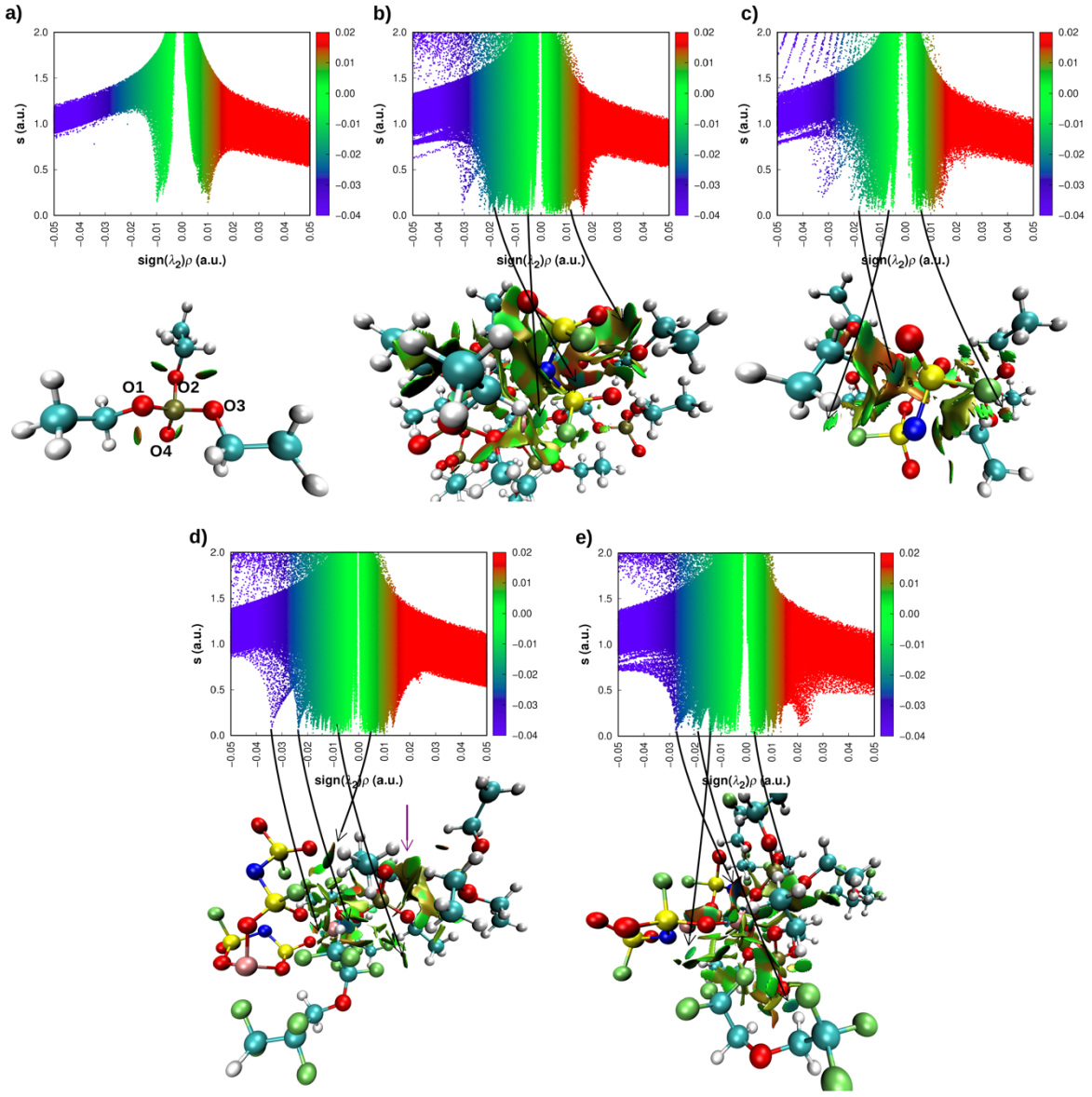

Figure S16. Reduced density gradient (RDG) plots (top) and the systems with isosurfaces corresponding to the colors of the scatter plots (bottom) for TEP molecule (a), 1.0 M LiFSI in TEP (b), 3.0 M LiFSI in TEP (c), 1.5 M LiFSI in TEP/TTE (d), and 1.5 M

LiFSI in TEP/BTFE (e). For all systems the isosurfaces were set to s=0.5 (a.u.). Green region, where ρ is close to zero, it indicates van der Waals interaction. Going down (up) to negative (positive) values of ρ, one has attractive (repulsive) interactions.

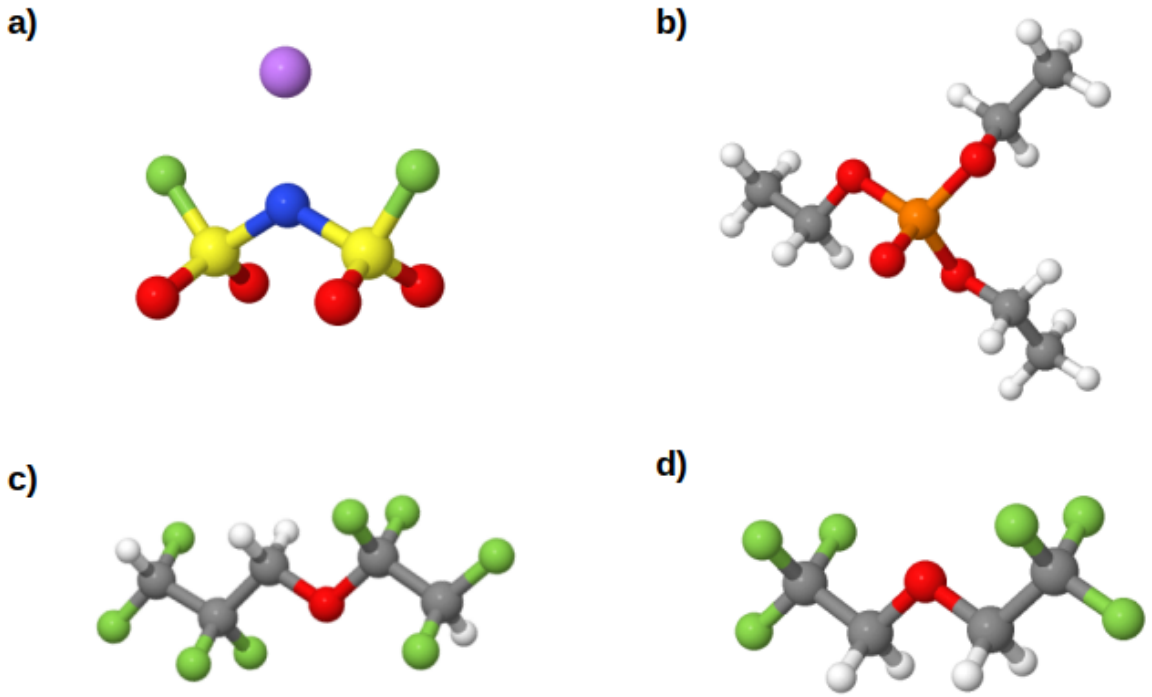

Figure S17 Atomic structures of the molecules that comprise the systems. Figures a), b), c), and d) show LiFSI, TEP, TTE, and BTFE, respectively. Purple, blue, yellow, green, red, orange, grey and white spheres stand for Li^+, nitrogen, sulfur, fluorine, oxygen, phosphorus, carbon and hydrogen.)

6 Electrochemical Performance

In-situ pressure evolution

In Figure S10 the *in-situ* pressure evolution graph is shown for one of the replicates of a) 1.5 M LiFSI in TEP/BTFE and b) 1.5 M LiFSI in TEP/TTE.

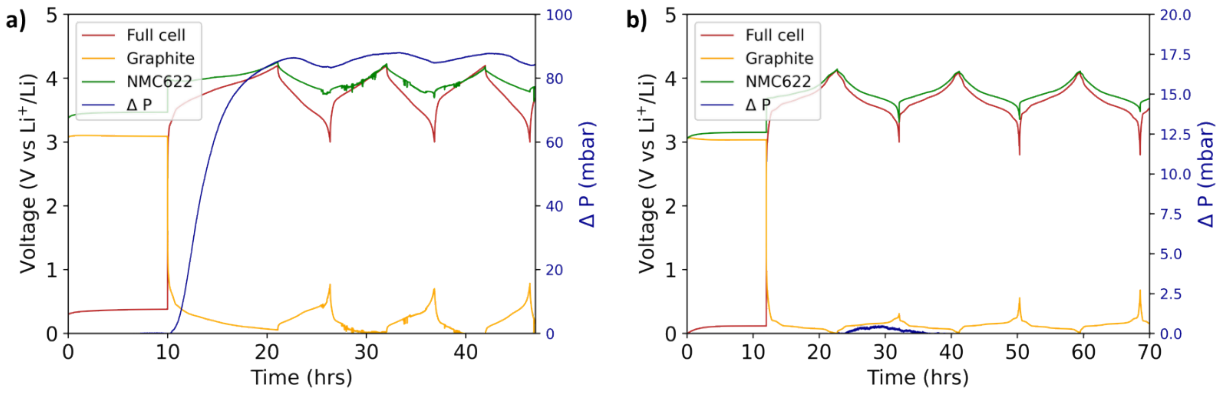

Figure S18. Replicate cells for pressure evolution in 3-electrode cells with NMC622 vs graphite (Li-metal reference), where a) 1.5 M LiFSI in TEP/BTFE shows significant pressure evolution, and b) 1.5 M LiFSI in TEP/TTE shows proper reproducibility.

Galvanostatic cycling in half-cells

The stability of the electrolyte was first analyzed in half-cells of Li|NMC622 and Li|Graphite. The initial coulombic efficiency (ICE) in NMC622 half-cells with BTFE based electrolyte was 86.8% and the discharge capacity after 50 cycles is 126 mAh/g. This is indicating proper capacity stability for 50 cycles for a new electrolyte, but still far from practical. The ICE in NMC622 half-cells with TTE based electrolyte was 85.4% and shows similar capacity fade as the BTFE based electrolyte. In Figure S10 the discharge capacities are shown for graphite half-cells. The capacity of the graphite used was 2.33 mAh/cm^2. Both LHCEs experience instabilities whilst cycling against

graphite. The BTFE based electrolyte however shows more stability over time, compared to the TTE based electrolyte. Although higher areal capacities were obtained in the TTE based electrolyte compared to the BTFE based electrolyte, this electrolyte also has short lifetime since it failed already after 10 cycles. The failure mechanism can possibly be explained by solvent intercalation and graphite exfoliation. So, from this experiment it is clear that the LHCEs show low areal capacities and are not showing promising compatibility with graphite anodes.

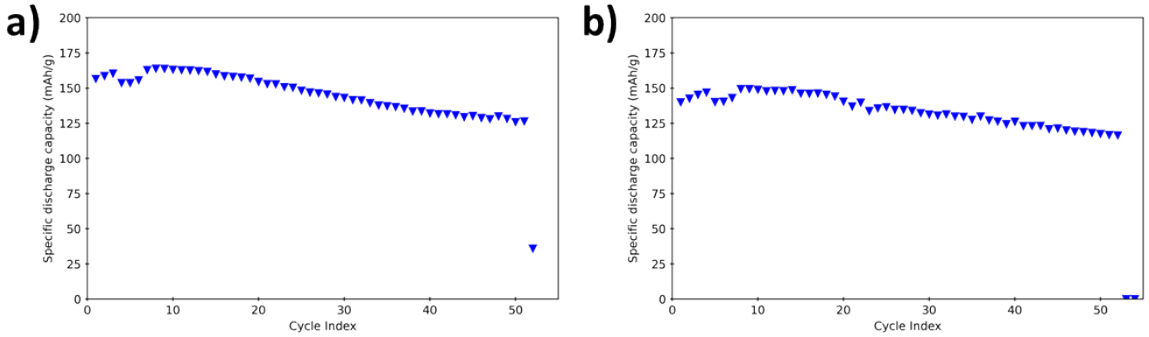

Figure S19. Discharge capacities of NMC622 half-cells. The left figure shows the discharge capacity versus cycles for a) 1.5 M LiFSI in TEP/BTFE electrolyte and b) 1.5 M LiFSI in TEP/TTE.

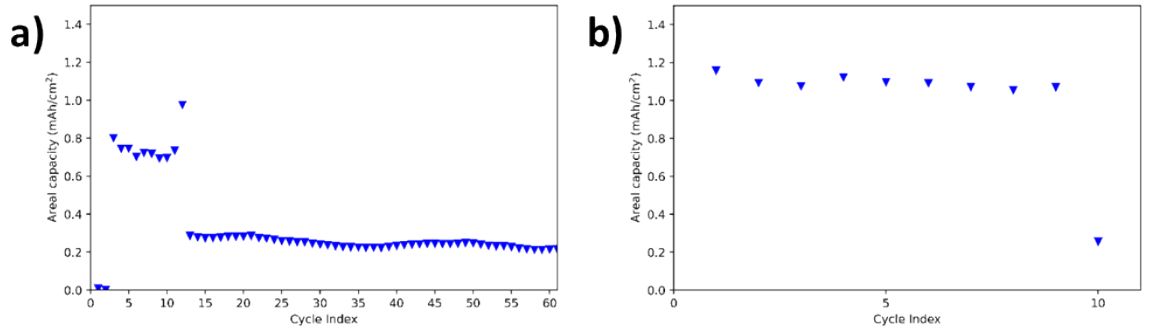

Figure S20. Discharge capacities of graphite half-cells. The left figure shows the discharge capacity versus cycles for a) 1.5 M LiFSI in TEP/BTFE electrolyte and b) 1.5 M LiFSI in TEP/TTE.

Plating and stripping efficiency

To evaluate the performance of the electrolyte in terms of plating and stripping, the reservoir method was applied which is described in more detail elsewhere. 23 The average plating and stripping efficiency of the BTFE and TTE based electrolyte were respectively 93.9% and 96.6%. The polarization at the lithium metal electrode is more severe in the BTFE electrolyte than in the TTE electrolyte, resulting in faster capacity fade. The polarization in the BTFE based electrolyte and the rather stable plating and stripping in the TTE based electrolyte can be observed in the potential versus time curve in Figure S12. The BTFE based LHCEs show lower CEs (93.9% vs 96.6%), faster polarization increase, and shorter cycle life in Li|Cu cells than the TTE based LHCEs. The insights on how solvent/diluent interactions affect Li-metal stability could provide important guidance for the future development of LHCEs.

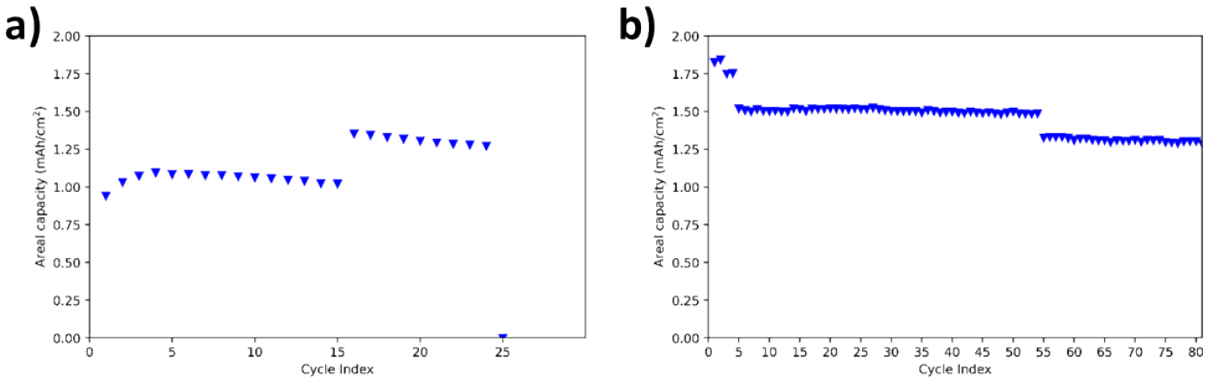

Figure S21. Areal discharge capacities of NMC622|graphite full-cells. The left figure shows the discharge capacity versus cycles for a) 1.5 M LiFSI in TEP/BTFE electrolyte and b) 1.5 M LiFSI in TEP/TTE.

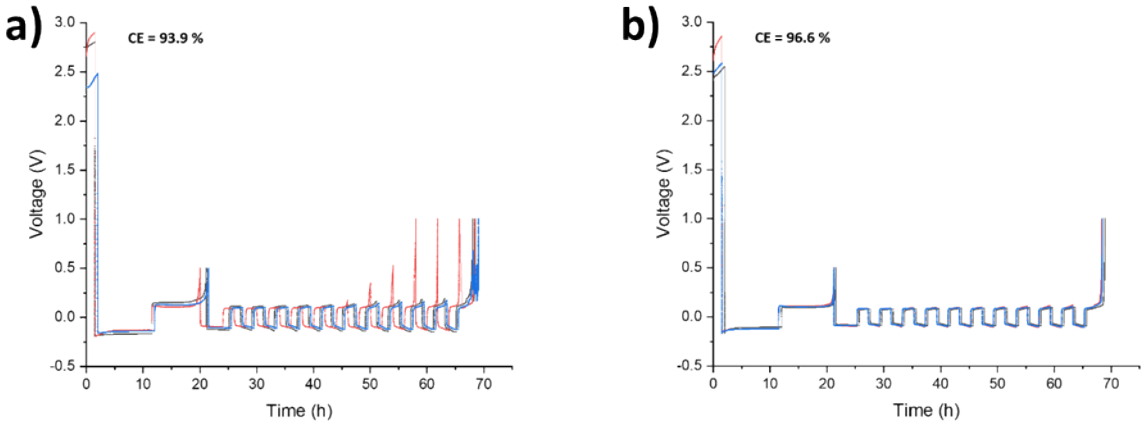

Figure S22. Charge/discharge curves of Li|Cu cells cycled at RT in a) 1.5 M LiFSI TEP BTFE and b) 1.5 M LiFSI TEP TTE (right).

References

1 S. Chen, J. Zheng, L. Yu, X. Ren, M. H. Engelhard, C. Niu, H. Lee, W. Xu, J. Xiao, J. Liu and J. G. Zhang, *Joule*, 2018, **2**, 1548–1558.

2 J. Wang, Y. Yamada, K. Sodeyama, C. H. Chiang, Y. Tateyama and A. Yamada, *Nat. Commun.*, 2016, **7**, 1–9.

3 K. Sodeyama, Y. Yamada, K. Aikawa, A. Yamada and Y. Tateyama, *J. Phys. Chem. C*, 2014, **118**, 14091–14097.

4 X. Fan, X. Ji, L. Chen, J. Chen, T. Deng, F. Han, J. Yue, N. Piao, R. Wang, X. Zhou, X. Xiao, L. Chen and C. Wang, *Nat. Energy*, 2019, **4**, 882–890.

5 H. Jia, L. Zou, P. Gao, X. Cao, W. Zhao, Y. He, M. H. Engelhard, S. D. Burton, H. Wang, X. Ren, Q. Li, R. Yi, X. Zhang, C. Wang, Z. Xu, X. Li, J. G. Zhang and W. Xu, *Adv. Energy Mater.*, 2019, **9**, 1–10.

6 X. Ren, S. Chen, H. Lee, D. Mei, M. H. Engelhard, S. D. Burton, W. Zhao, J. Zheng, Q. Li, M. S. Ding, M. Schroeder, J. Alvarado, K. Xu, Y. S. Meng, J. Liu, J. G. Zhang and W. Xu, *Chem*, 2018, **4**, 1877–1892.

7 X. Ren, L. Zou, X. Cao, M. H. Engelhard, W. Liu, S. D. Burton, H. Lee, C. Niu, B. E. Matthews, Z. Zhu, C. Wang, B. W. Arey, J. Xiao, J. Liu, J. G. Zhang and W. Xu, *Joule*, 2019, **3**, 1662–1676.

8 X. Zhang, L. Zou, Y. Xu, X. Cao, M. H. Engelhard, B. E. Matthews, L. Zhong, H. Wu, H. Jia, X. Ren, P. Gao, Z. Chen, Y. Qin, C. Kompella, B. W. Arey, J. Li, D. Wang, C. Wang, J. G. Zhang and W. Xu, *Adv. Energy Mater.*, 2020, **10**, 1–11.

9 Q. K. Zhang, X. Q. Zhang, L. P. Hou, S. Y. Sun, Y. X. Zhan, J. L. Liang, F. S. Zhang, X. N. Feng, B. Q. Li and J. Q. Huang, *Adv. Energy Mater.*, 2022, **12**, 2200139

10 H. Jia, Y. Xu, X. Zhang, S. D. Burton, P. Gao, B. E. Matthews, M. H. Engelhard, K. S. Han, L. Zhong, C. Wang and W. Xu, *Angew. Chemie - Int. Ed.*, 2021, **60**, 12999–13006.

11 H. Jia, Y. Xu, S. D. Burton, P. Gao, X. Zhang, B. E. Matthews, M. H. Engelhard, L. Zhong, M. E. Bowden, B. Xiao, K. S. Han, C. Wang and W. Xu, *ACS Appl. Mater. Interfaces*, 2020, **12**, 54893–54903.